CrossMark

Instabilities along the Axis of the Heliospheric Jets

Xiaohan Ma[1] , Merav Opher[1] , Marc Kornbleuth[1] , and Gabor Toth[2]
[1] Boston University, USA
[2] University of Michigan, USA

Abstract

The heliosphere is influenced by the interaction of neutral hydrogen atoms from the interstellar medium with protons in the heliosheath (HS). The confinement by the solar magnetic field of the HS plasma forms distinct north and south heliospheric jets. Previous global MHD simulations of the heliosphere reveal that instabilities can develop in the heliospheric jets and make them become unstable, giving rise to large-scale turbulence. In this study, we show that there is a low-speed region of solar wind in the HS that provides a precondition for instabilities to develop. The low-speed region is formed due to charge exchange and magnetic tension. This region allows sufficient time for the instabilities to develop and induces a shear flow inside the HS leading to the development of a Kelvin–Helmholtz (K-H) instability. The estimated growth timescale of the K-H instability based on the simulation results is around 5–7 yr. Understanding the development of the instabilities in the HS is crucial for comprehending the dynamic processes within the HS and the structure of the heliosphere.

1. Introduction

There is an ongoing debate on the shape and structure of the heliosphere, the outer region surrounding the Sun where the solar wind extends. Previously, the shape of the heliosphere was thought to be comet-like with a tail extending to thousands of astronomical units (E. N. Parker 1961; V. B. Baranov et al. 1976). The recent modeling, however, suggests that the heliosphere may have a short split-tail structure (J. F. Drake et al. 2015; M. Opher et al. 2015, 2020). G. Yu (1974) suggested a two-lobe structure of the heliosphere's tail. Works such as M. Opher et al. (2015) argue that the tension of the solar magnetic field is comparable to the pressure gradients in the heliosheath (HS) and will resist stretching. Their numerical simulations show that the magnetic tension of the solar magnetic field, which has a spiral structure, deflects the HS flows, confining them to two lobes of the heliosphere's tail, known as heliospheric jets. The analytic work of J. F. Drake et al. (2015) shows that indeed the magnetic tension in the radial direction deflects the flows to the north and south. Such confinement was seen as well in works such as N. V. Pogorelov et al. (2015), V. V. Izmodenov & D. B. Alexashov (2015), E. A. Golikov et al. (2016), and M. Kornbleuth et al. (2021), especially when the Mach number of the interstellar flow is small (S. Korolkov & V. Izmodenov 2021). However, these models do not reach a consensus on how far down the tail this two-lobe feature extends and whether the surrounding interstellar medium (ISM) can penetrate the region between the two lobes.

Physical processes in the tail of the solar wind interaction region with the partially ionized local ISM have long been discussed. The charge exchange process between hydrogen atoms and plasma protons can affect the structure of the

heliosphere's tail (V. V. Izmodenov & D. B. Alexashov 2003; J. Kleimann et al. 2022). Global MHD simulations of the heliosphere reveal that heliospheric jets can become unstable in the heliotail region, giving rise to large-scale turbulence (M. Opher et al. 2015; N. V. Pogorelov et al. 2015; M. Opher et al. 2020, 2021). This turbulence inside the HS has the potential to enhance magnetic reconnections, and also disrupt the coherence of the heliospheric jets. This can facilitate the penetration of ISM material into the heliospheric tail, contributing to the development of the short and separate heliotail. Consequently, pinning down the drivers of the turbulence is crucial for understanding the structure and shape of the heliosphere. M. Opher et al. (2021) argued that the instabilities within the HS along the axis of the heliospheric jets may serve as the key to understanding the mechanisms driving turbulence development.

Previous studies of heliosphere instabilities were all focused at the heliopause (HP). Since the interstellar plasma is much denser than the HS plasma, a Rayleigh–Taylor–like instability occurs along the HP (P. Liewer et al. 1996; G. P. Zank et al. 1996; G. P. Zank 1999) due to the effective gravity produced by neutral atoms charge-exchanging with and, therefore, dragging the plasma ions. The effective gravity depends on the neutral density, velocities, and charge-exchange cross section. Furthermore, V. Florinski et al. (2005) and K. Avinash et al. (2014) expanded the analysis to include the stabilizing effect of hot HS neutrals. Meanwhile, the shear flow arising from the velocity disparity between the HS and interstellar flows drives Kelvin–Helmholtz (K-H)–like modes at the HP (V. Baranov et al. 1992; S. V. Chalov 1996; K. Avinash et al. 2015). V. Baranov et al. (1992) investigated the stability of the HP boundary, showing that K-H instabilities are expected in the flanks of HP, with instability dependent on the perturbation wavevector angle and density ratio across the HP. S. V. Chalov (1996) also showed that the nose of the HP is unstable to short-wave disturbances, while a periodic change of the stellar

wind dynamic can reduce the K-H instability at the HP (S. D. Korolkov & V. V. Izmodenov 2022).

Due to the interaction of neutral hydrogen atoms from the ISM with ions in the HS, instabilities may also occur within the HS. M. C. Begelman (1998) proposed that the kink instability plays a pivotal role in driving turbulence in astrophysical jets. N. V. Pogorelov et al. (2015) and F. Fraternale et al. (2023) argued that a kink instability is what drives the turbulence in the heliosphere's tail. Recent research by M. Opher et al. (2021) revealed the magnetic field structure and velocity shear within the heliospheric jets serve as stabilizing factors, preventing the occurrence of kink or sausage instabilities. M. Opher et al. (2021) argued that there is a Rayleigh–Taylor instability produced by the interaction of neutral hydrogen (H) atoms streaming from the ISM with the ionized matter inside the HS along the axis of heliospheric jets. The charge-exchange interaction between neutral hydrogen atoms and solar wind ions acts as an effective gravitational force. Additionally, due to the confinement of the solar wind by the solar magnetic field, there exists a density gradient perpendicular to this axis. M. Opher et al. (2021) suggested that these factors collectively contribute to the development of the instability along the axis of the heliospheric jets. The timescale of this instability depends on the density of neutral H in the ISM, and for typical values, the estimated growth timescale is ∼3 yr. In this paper, we examined the development of K-H instability in the HS instead of the HP.

This paper is organized as follows: We describe the magnetohydrodynamic (MHD) model used for the simulations in Section 2. Section 3 discusses the formation of the low-speed region and the presence of the K-H instability in the HS. Finally, in Section 4 we present discussions and conclusions.

2. Numerical Model

We use the same MHD model as M. Opher et al. (2021), which is briefly described in Section 2.1. In Section 2.2, we describe the grid resolutions and the different setups used in the current simulation.

2.1. Single-ion Model

The MHD model of the outer heliosphere (OH) components uses the Space Weather Modeling Framework (SWMF; G. Tóth et al. 2012). The SWMF includes the Block-Adaptive Tree Solar wind Roe-Type Upwind Scheme (BATS-R-US) solver (G. Tóth et al. 2012), a 3D block-adaptive, upwind finite-volume MHD code that is highly parallel. BATS-R-US can solve steady-state as well as time-accurate problems using different time-stepping algorithms. Local time stepping speeds up the convergence to a steady state by setting different time steps for each grid cell based on the local stability condition, while time-accurate simulations use the same time step for all grid cells (G. Tóth et al. 2012).

M. Opher et al. (2003) adapted BATS-R-US to the OH as the OH component of SWMF. The OH component is capable of treating multiple ion fluids (M. Opher et al. 2020) in addition to multiple neutral fluids (M. Opher et al. 2009). Here we use only a single-ion fluid as used in M. Opher et al. (2015) and M. Opher et al. (2021), where the cold thermal solar wind and hot pickup ions (PUIs) are treated as a single species (G. P. Zank 1999; M. Opher et al. 2015, 2021). The neutral H component is represented using a four-fluid approximation

(G. P. Zank 1999; M. Opher et al. 2009). The coordinate system is such that the z-axis is parallel to the solar rotation axis, the x-axis is oriented such that the interstellar flow is in the x–z plane and pointing 5° upward of the x-axis, and the y-axis completes the right-handed coordinate system.

For the inner boundary parameters at 30 au, we maintain the same values for solar wind as M. Opher et al. (2021). The solar wind parameters, speed, density, and temperature, are set as $U_{SW} = 417 \, \mathrm{km \, s^{-1}}$, $n_{SW} = 8.74 \times 10^{-3} \, \mathrm{cm^{-3}}$, and $T_{SW} = 1.087 \times 10^5 \, \mathrm{K}$, respectively. For the magnetic field of the solar wind, we used the Parker spiral magnetic field model proposed by E. N. Parker (1958) with $B_{SW} = 7.17 \times 10^{-3} \, \mathrm{nT}$ at the equator. To minimize artificial reconnection effects, we adopt a monopole configuration for the solar magnetic field, aligning it with the solar rotation axis as in M. Opher et al. (2015). The solar wind flow at the inner boundary is assumed to be spherically symmetric.

The parameters of ISM conditions are the same as in M. Opher et al. (2021). The ISM plasma density and temperature are $n_{ISM} = 0.06 \, \mathrm{cm^{-3}}$ and $T_{ISM} = 6519 \, \mathrm{K}$, respectively. The magnetic field of ISM in the model is $B_{ISM} = 4.4 \, \mu\mathrm{G} = 0.44 \, \mathrm{nT}$, only in the z-direction. The hydrogen atoms in the ISM have a number density $n_H = 0.18 \, \mathrm{cm^{-3}}$ and a temperature the same as that of the interstellar plasma. The speed of the neutral H atoms was set to 26.4 km s^{-1} in the x-direction.

2.2. Grid Resolution

To avoid the initial numerical transients that may affect the analysis of instability, we initiate the model with a coarse grid resolution as shown in Figure 1. Around the termination shock (TS), the cell size is set to 12 au, which can damp any initial numerical instability inside the HS. The coarse grid resolution precludes the development of instabilities.

We initially run the model with a coarse grid and without charge exchange using local time stepping for 30,000 steps and then run in accurate-time mode for 50 yr until it reaches a steady state as described in Section 2.1. These model results are shown in Figure 2 (left panels). Subsequently, we turn on the charge exchange, and continue the simulation for another 500 yr when the heliosphere is fully in steady state. During this time, a low-speed region of solar wind formed inside the HS, as depicted in the right panels of Figure 2 and in Figure 3. We use the simulation results to explain the formation of the low-speed region in Section 3.1.

In Section 3.2, to analyze instabilities inside the HS, we reduced the grid size to approximately 2 au inside the HS. Before the grid refinement, initial numerical transients had already completed the evolution and dissipated, while the heliosphere had achieved a steady state. After the grid was refined, the development of instabilities in the HS can appear in the model results.

3. Result

3.1. Formation of the Low-speed Region

As described in Section 2.2, we initially run a model without charge exchange and then turn on charge exchange. Figure 2 depicts the results of the HS under the steady-state condition before charge exchange was turned on (left panels), and the results after running for an additional 32 yr following charge-exchange activation (right panels). Figures 2(A)–(B) present the solar wind speed within a large region ($-500 \, \mathrm{au} < X < 1500 \, \mathrm{au}$, $-500 \, \mathrm{au} < Z < 1000 \, \mathrm{au}$) that encompasses almost the entire

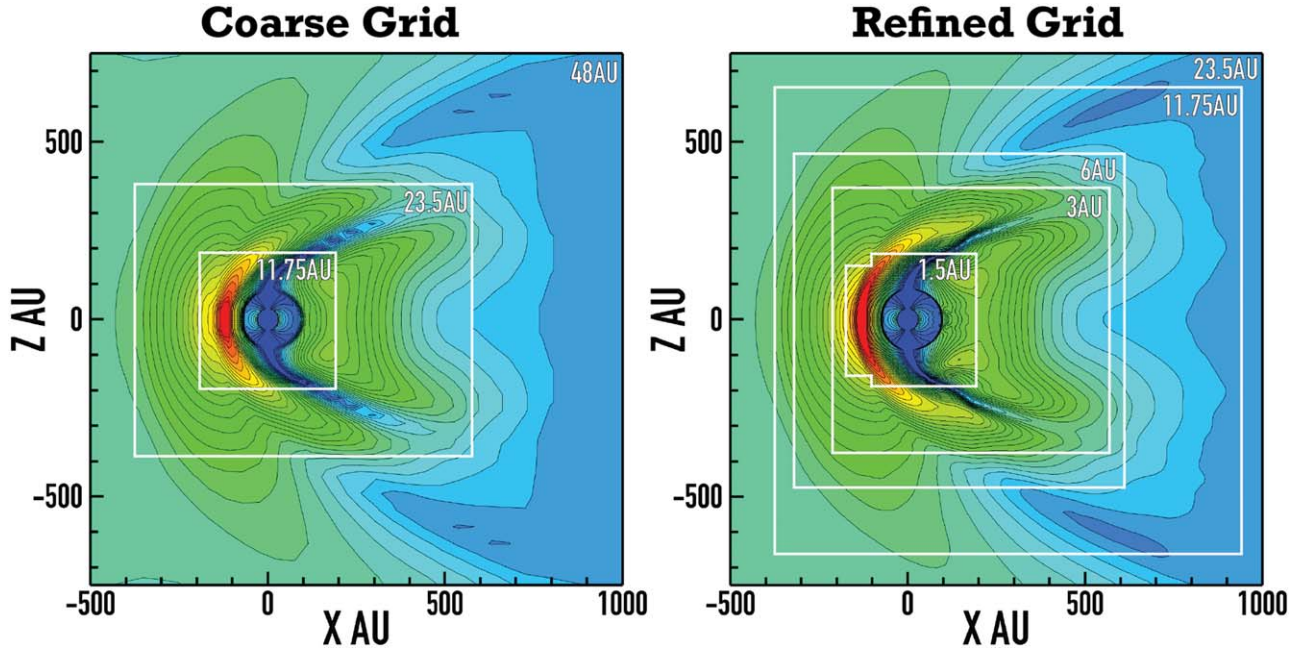## Coarse Grid   Refined Grid

Figure 1. Comparison of the coarse and fine grids used in our simulations. The colors show the magnetic field. The white lines show the grid resolution changes and the white labels indicate the grid cell size in each region.

heliosphere. The HP boundaries are indicated by the white lines, defined by the temperature of solar wind $T = 50,000$ K. The area outlined in black is zoomed in and shown below. As illustrated in Figures 2(A) and (C), without charge exchange, the solar wind speed in the HS is approximately $120 \, \mathrm{km \, s^{-1}}$. After charge exchange is turned on, the solar wind speed begins to decrease, especially near the axis of the heliospheric jet where the minimum speed reaches approximately $20 \, \mathrm{km \, s^{-1}}$ as shown in Figures 2(B) and (D). Without charge exchange, the solar wind density is notably lower inside the HS, decreasing inward from the nose of the HP as shown in Figure 2(E). However, after charge exchange is turned on, the solar wind density increases within the HS and becomes extremely high near the axis of the heliospheric jet as shown in Figure 2(F). The axis of the heliospheric jet can be seen as the region where the magnetic field is nearly zero in Figures 2(G) and (H). When charge exchange is turned on, the TS shrinks from 270 to 80 au in the tail as shown in Figures 2(C) and (D). As a result of the contraction, the solar magnetic field in the HS becomes at least 3 times stronger compared to that in the HS without charge exchange as shown in Figures 2(G) and (H).

The solar wind flow within the HS is influenced by the gradient of thermal pressure, the gradient of magnetic pressure, the magnetic tension, and the charge-exchange source terms. The momentum equation of the solar wind can be written as

$$\rho \frac{D\boldsymbol{U}}{Dt} = \rho \left(\frac{\partial}{\partial t} + \boldsymbol{U} \cdot \nabla \right) \boldsymbol{U} = \boldsymbol{J} \times \boldsymbol{B} - \nabla P + \boldsymbol{S}_{\mathrm{CX}}$$
$$= \frac{(\boldsymbol{B} \cdot \nabla)\boldsymbol{B}}{\mu_0} - \nabla \left(\frac{B^2}{2\mu_0} \right) - \nabla P + \boldsymbol{S}_{\mathrm{CX}}$$
$$= \boldsymbol{F}_{\mathrm{T}_B} + \boldsymbol{F}_{\mathrm{P}_B} + \boldsymbol{F}_{\mathrm{P}} + \boldsymbol{S}_{\mathrm{CX}}, \qquad (1)$$

where ρ is the density and $\boldsymbol{U}$ is the velocity. The first term on the right-hand side is the magnetic tension ($\boldsymbol{F}_{\mathrm{T}_B} = (\boldsymbol{B} \cdot \nabla)\boldsymbol{B}/\mu_0$), the second term is the gradient of magnetic

pressure ($\boldsymbol{F}_{\mathrm{P}_B} = -\nabla \left(\frac{B^2}{2\mu_0} \right)$), the third term is the gradient of thermal pressure ($\boldsymbol{F}_{\mathrm{P}} = -\nabla P$), and the fourth term is the momentum source term from charge exchange ($\boldsymbol{S}_{\mathrm{CX}}$) between the solar wind protons and ISM neutral H.

Figures 3(D)–(F) show the ratio of different terms on the right-hand side of Equation (1) to the solar wind momentum along the parallel component of solar wind velocity. Negative values indicate a deceleration of the solar wind, while positive values indicate acceleration. Panel (F) illustrates how the solar wind speed changes over time during the 10–40 yr at point B, after the onset of charge exchange, and also how these components vary with time. The ratio of the total momentum variation ($\rho \frac{D\boldsymbol{U}}{Dt}$) to the momentum itself is shown as the purple curve. The value is negative for the first 35 yr after charge exchange begins, indicating the solar wind speed keeps decreasing after the charge exchange is turned on. The momentum source term due to the charge exchange between the solar wind and neutral H dominates the deceleration of the solar wind speed for the first 18 yr of charge exchange.

Figures 3(A)–(C) show the results of solar wind speed, magnetic field, and solar wind density 24 yr after charge exchange was turned on. Within the heliospheric jet, the magnetic field magnitude remains negligible at the axis (where the magnetic field $B < 0.05$ nT). The heliospheric jet is bent due to the interaction between the solar wind and neutral hydrogen, causing the magnetic field lines (gray ribbons) to be not perpendicular to the solar wind streamline (black line) as shown in Figure 3(C). Magnetic tension strength confines more solar wind plasma along the jet axis as shown in Figure 3(C), where the solar wind density is higher near the axis. We take a line cut through the heliospheric jet as shown in Figure 3(D). One can see that in Figure 3(D), along the line cut from A to C, the solar wind speed first decreases and then increases, with point B representing the lowest solar wind speed. The total momentum variation is the largest at point B, and the combined effects of charge-exchange source term and magnetic tension
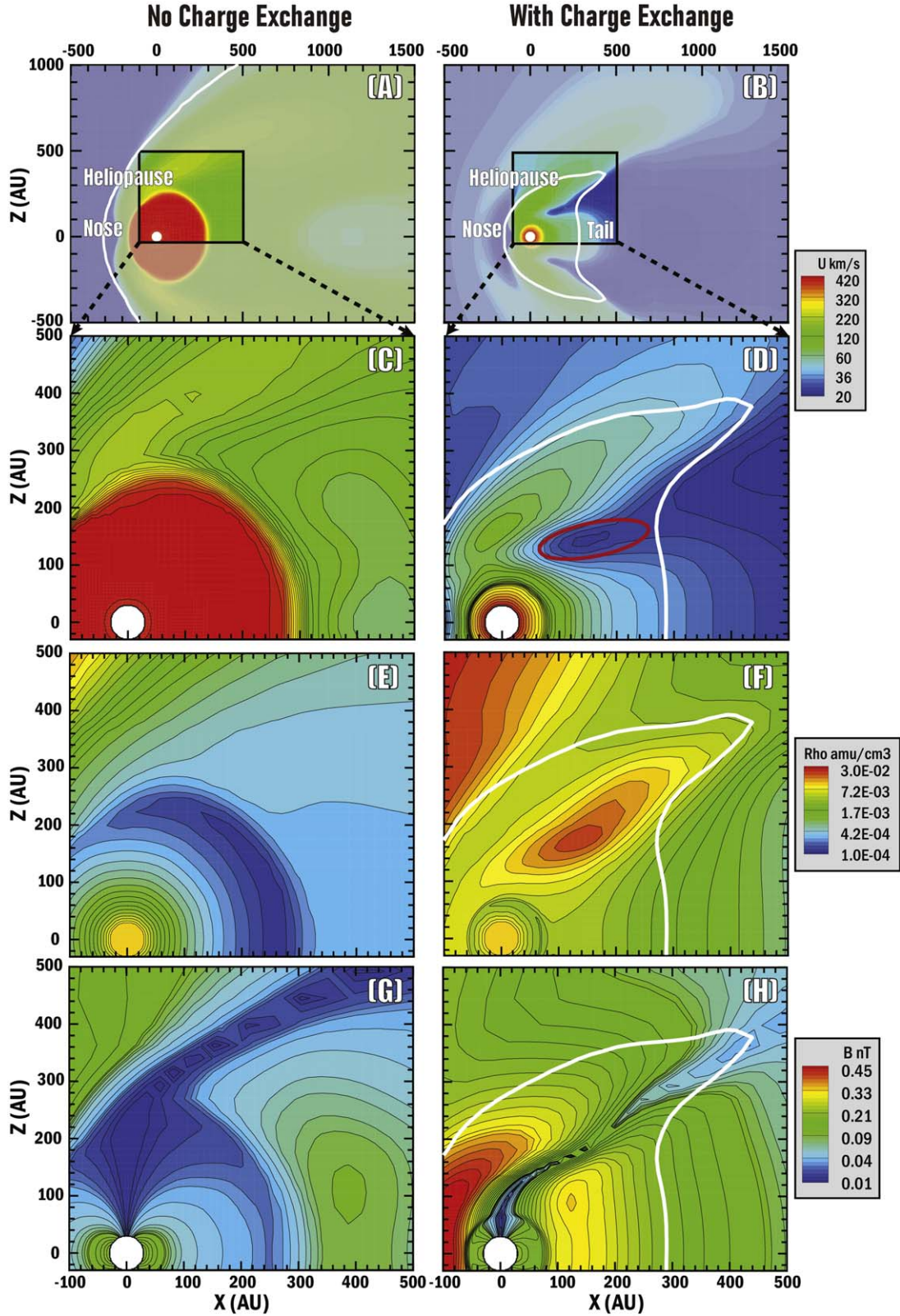
Figure 2. Contours of solar wind speed (A)–(D), density (E)–(F), and magnetic field (G)–(H) in the meridional plane without charge exchange (left) and 32 yr after charge exchange is turned on (right). The white lines represented the HP boundary, defined by $T = 50,000$ K. The area outlined by the black solid line in (A) and (B) has been zoomed in for panels (C) and (D). The low-speed region is encircled by a red line in panel (D).

have the greatest influence on decreasing the solar wind speed there. Among these factors contributing to the decrease, magnetic tension has the most significant effect.

The bent heliospheric jet creates an angle between the magnetic field lines and the solar wind streamlines as shown in Figure 3(C), resulting in the magnetic tension having a component parallel to the
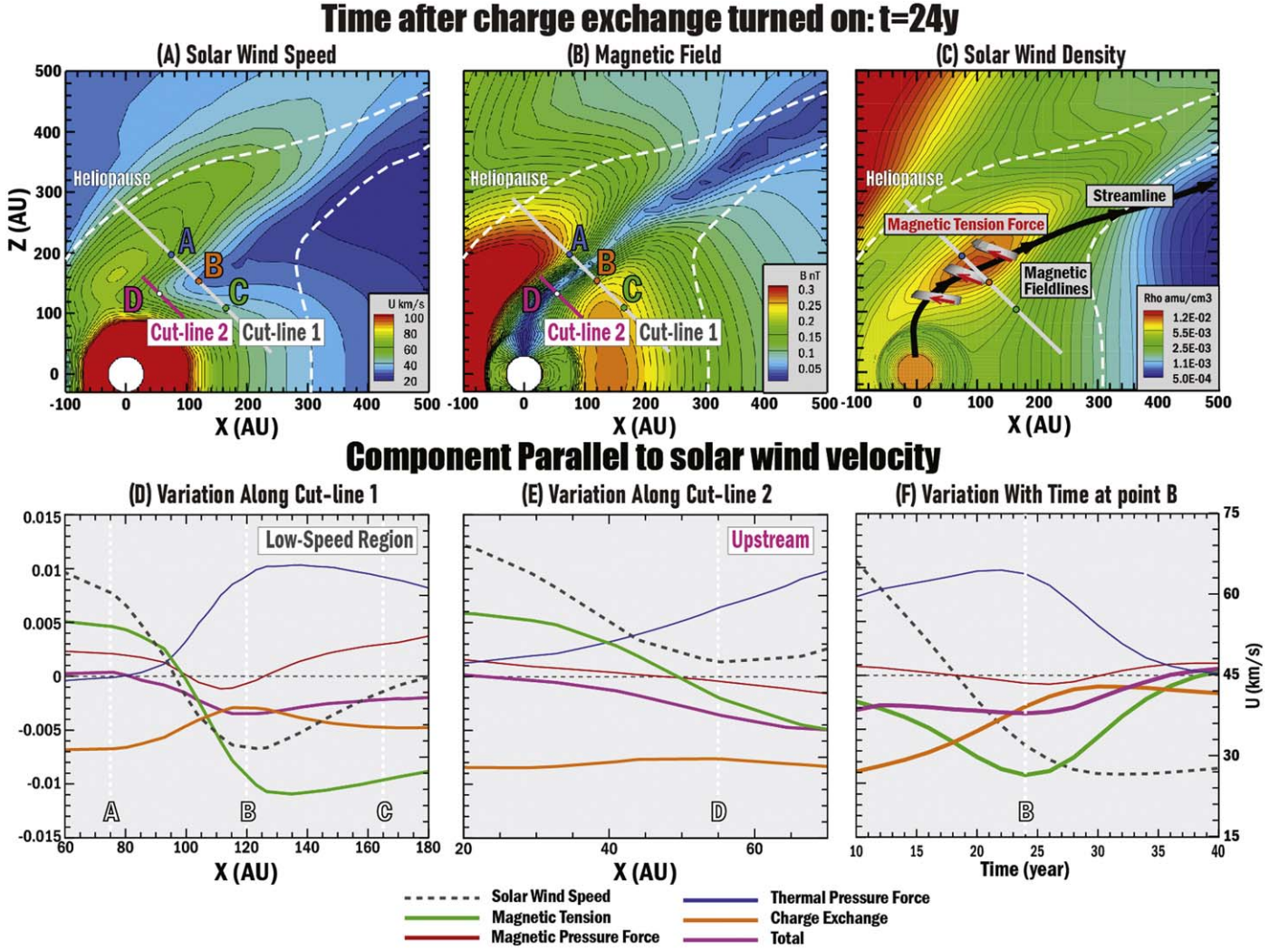
Figure 3. (A)–(C) Contours of solar wind speed, magnetic field strength, and solar wind density 24 yr after charge exchange was switched on. The direction of the magnetic tension force is shown as the red arrows, and the solar wind streamline is shown as the black line; the magnetic field lines are shown as gray ribbons in panel (C). The white dashed lines represent the HP boundary, defined by $T = 50,000$ K. (D)–(F) The ratio of the parameters on the right-hand side of Equation (1) parallel to the solar wind momentum (ρU). Negative values indicate a deceleration of the solar wind, while positive values indicate acceleration. Panel (D) shows the results along the gray cut-line through the heliospheric jet at the low-speed region. Panel (E) shows the results along the pink cut-line at the upstream. Panel (F) are the results at point B as a function of time after charge exchange is turned on. The black dashed curves represent the change of total solar wind speed over time. The green, red, blue, orange, and purple curves represent the magnetic tension, the gradient of magnetic pressure, the gradient of thermal pressure, the charge exchange source term, and the total effect of these terms parallel to the solar wind velocity, respectively.

solar wind on one side (point A) and a component antiparallel to the solar wind on the other side (points B and C). The axis lies between points A and B, so from point A to the axis, the positive magnetic tension force increases the solar wind speed from point A to the axis, and from the axis to point B the negative magnetic tension decreases the solar wind speed as shown in Figure 3(D). From point B to point C, the magnitude of magnetic tension decreases causing the influence on the solar wind speed also decreases. Meanwhile, the magnetic tension strength confines more solar wind plasma along the jet axis as shown in Figure 3(C), causing the charge exchange rate to be higher at point A than at point B. Therefore, the higher rate of charge exchange, resulting in an enhanced trend of speed reduction, counteracts the trend of speed increase induced by the magnetic tension. As shown in Figure 3(D), upstream of the low-speed region, the force from charge exchange acts in the opposite direction of the solar wind, suggesting a tendency for the solar wind to slow down. The magnetic tension force is not strong enough as in the low-speed region, acting in the same direction as the solar wind on the left side

of point D, which mitigates the deceleration of the solar wind speed. At point D, the solar wind speed is 47.7 km s^{-1}, while at point B, it decreases to 31.8 km s^{-1}. As a result, the magnetic tension force decreases the solar wind speed more significantly at point B, finally creating a low-speed region around the point.

Figure 4 shows the model results after charge exchange was turned on. They reveal the absence of any instability in the HS with the coarse grid and the existence of a low-speed region. Figures 4(D)–(F) represent the solar wind speed of the stable heliosphere. The results obtained in the X–Z plane and the Y–Z plane show the existence of a distinct low-speed region in a 3D elliptical shape as shown in Figure 4(F). This low-speed region induces velocity shear that can lead to the K-H instability.

3.2. K-H Instability

Section 2.2 describes how the coarse-grid model is refined after reaching a steady state, allowing the model to detect small-scale changes with higher resolution. This refinement
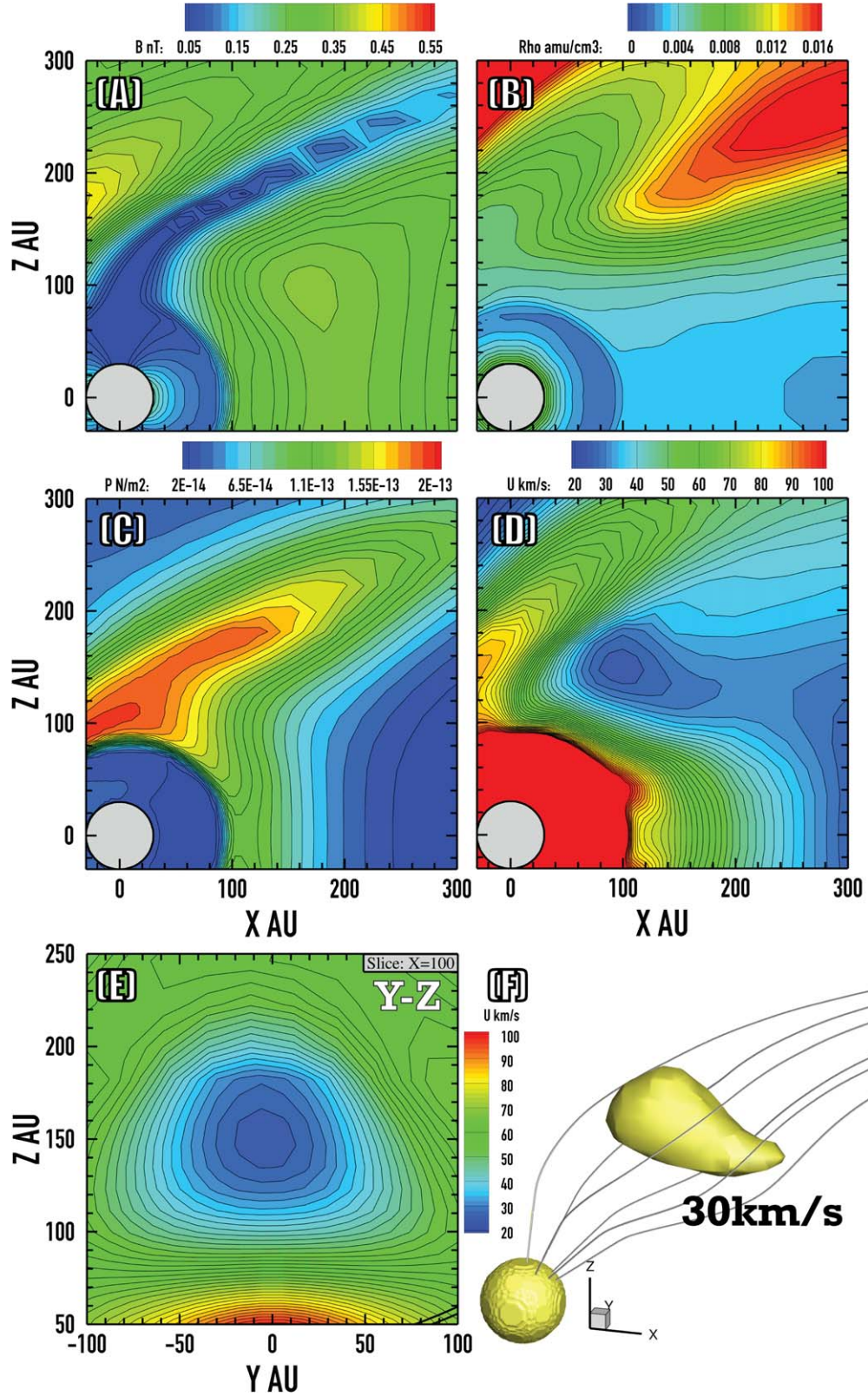
Figure 4. The single ion model results in a steady state after charge exchange is turned on. (A)–(C) show the contours of magnetic field (A), density (B), and thermal pressure of solar wind ions (C). (D)–(F) show the contours of solar wind speed in the X–Z plane (D) and the Y–Z plane (E) and the yellow iso-surface of $U = 30$ km s^{-1} (F). The gray lines in panel (F) are streamlines of solar wind ions in the HS.

allows for the development of instabilities within the HS. Figure 5 presents the effect of grid refinement on instabilities in the heliosphere. Figure 6 presents the 3D results following the grid refinement. The solar wind streamlines represented by the gray lines show the morphology and direction of this shear flow, as shown in Figures 6(A1)–(A3).
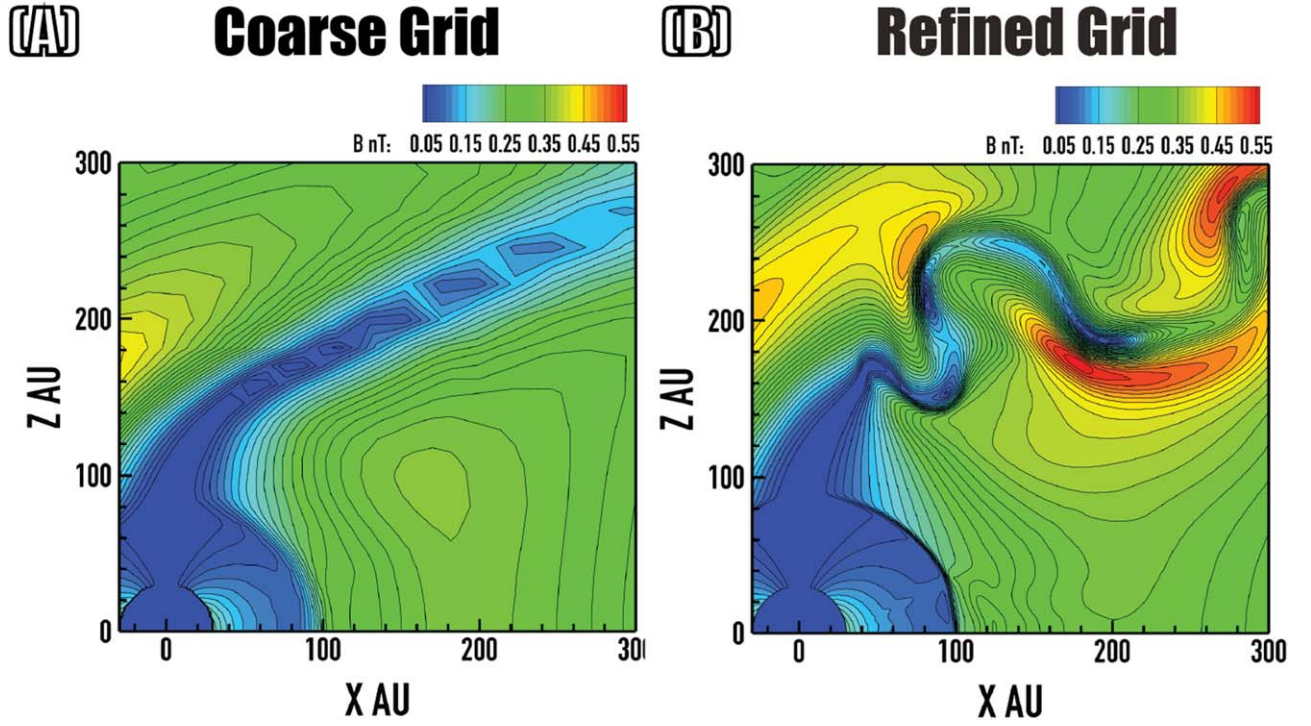
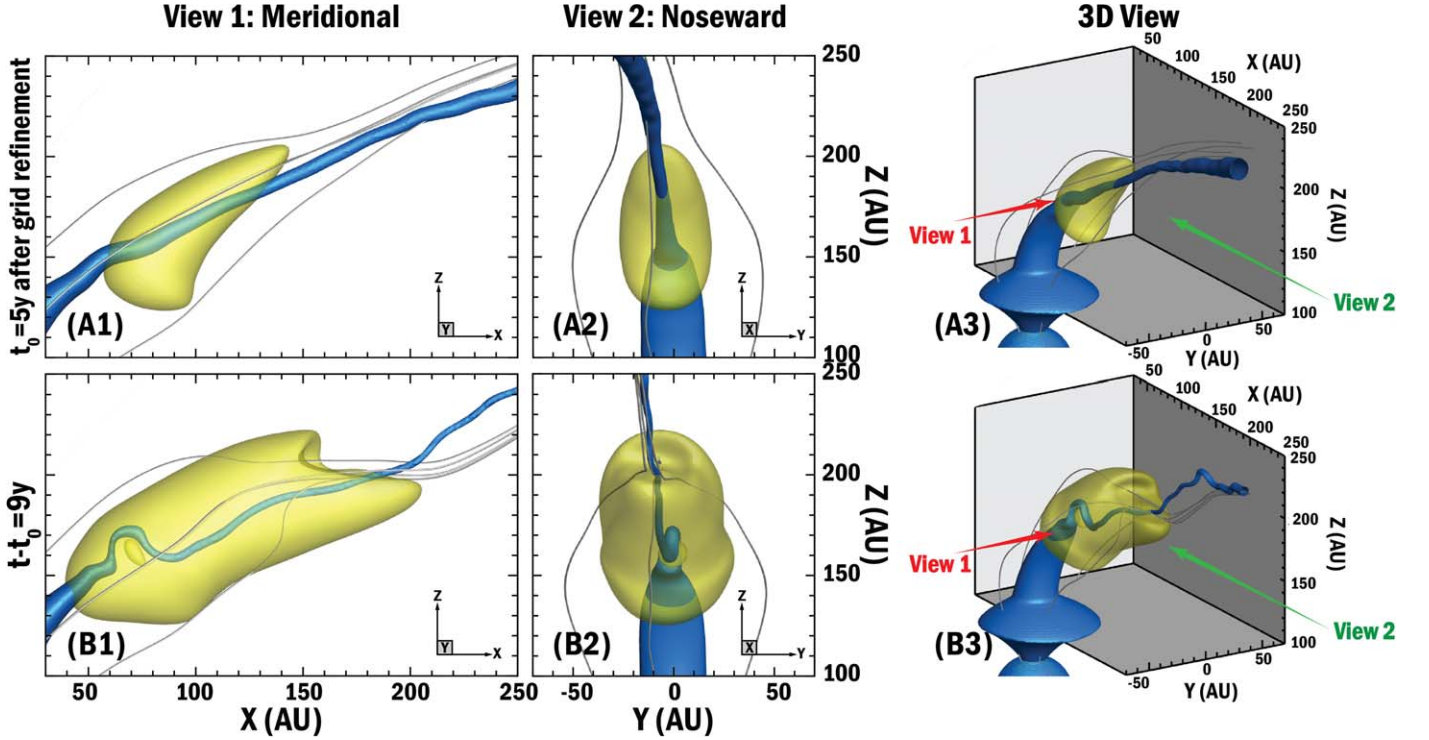**Figure 5.** Contours of solar magnetic field in the meridional plane before and after the grid refinement.

Figure 6. (A) The MHD results 5 yr after the grid is refined and the initial time when instability begins (t_0). (B) The results 9 yr later. The blue iso-surfaces represent the region where the magnetic field strength, B, is at 0.07 nT, indicating the axis of the heliospheric jet. The yellow iso-surfaces represent the region where the solar wind speed is 20 km s^{-1}. The gray curves represent the solar wind streamlines. From left to right, the view planes are meridional (view 1) and noseward (view 2), respectively. The right panels show the 3D view of the low-speed region structure.

The low-speed region continues to expand over time after grid refinement, as shown in the comparison with panels (A) and (B). Due to the influence of instability, its shape becomes more irregular, leading to distortion in the solar wind streamlines as shown in panels (B1)–(B3) of Figure 6. In the

meridional plane, the instabilities grow perpendicular to the axis as shown in Figure 6(B1). Simultaneously, from the noseward views, the axis of the heliospheric jet is distorted, as shown in Figure 6(B2), indicating the occurrence of additional instabilities developing along the direction of solar wind

magnetic field lines in the azimuthal direction. The presence of shear flows due to the low-speed region results in K-H instability.

Figure 7 illustrates an alternative view of the velocity shear within the HS after the grid refinement at the same time as Figures 6(A1)–(A3). The shear flow is induced by the low-speed region of the solar wind. The 3D view displays the axis of the heliospheric jet and the low-speed region, along with a cross sectional profile perpendicular to the axis. Figure 7(B) presents the total solar wind speed in the cross sectional view perpendicular to the heliospheric jet. These results show the velocity increases outward from the axis. This leads to the formation of shear flow within the solar wind, thereby resulting in the generation of a K-H instability within the HS. Figure 7(C) displays the solar wind density and speed along the line-cut through the heliospheric jet in the Y-direction, and Figure 7(D) displays the solar wind density and speed along the cross section in the X–Z plane perpendicular to the heliospheric jet. The directions are illustrated in Figure 7(A).

A. Miura & P. L. Pritchett (1982) conducted a detailed parameter study, demonstrating that short-wavelength (large wavenumber) instabilities are suppressed in cases of gradual velocity shear. They also found that for a finite shear layer width, the growth rate is consistently below the theoretical K-H instability growth rate calculated in S. Chandrasekhar (1961):

$$\gamma = \frac{\sqrt{\rho_i \rho_o}}{\rho_i + \rho_o} \cdot k \cdot \Delta U. \qquad (2)$$

In our analysis, we use this formula as an upper estimate of the growth rate, given the complex geometry and the varying velocity shear along the jet. In this formula, i and o means inside and outside of the tube, respectively, as shown in Figure 7(C), ΔU is the speed difference, $k = 2\pi/\lambda$ is the wavenumber, and $\lambda \approx 70$ au is the wavelength of the perturbation along the jet. From Figure 7(C) the solar wind speed results, we can get, $U_i = 10.8$ km s^{-1} and $\overline{U_o} = 70.9$ km s^{-1}, then $\Delta U = 60.1$ km s^{-1}. Considering $\rho_i = 0.0163$ amu cm^{-3}, $\bar{\rho}_o = 0.0055$ amu cm^{-3}, the growth rate $\gamma = 0.49$ yr^{-1}, and the growth timescale of K-H instability in the Y-direction is around 2.1 yr derived from theoretical calculation.

In the meridional cross section, Figure 7(D), we take the velocity shear with the larger jump on the $L < 0$ side as it will determine the growth rate. Here $U_i = 10.8$ km s^{-1} and $U_{o2} = 87.5$ km s^{-1}, so $\Delta U = 76.7$ km s^{-1}, $\rho_i = 0.0163$ amu cm^{-3}, and $\rho_{o2} = 0.007$ amu cm^{-3}. Using these values, the growth rate $\gamma = 0.66$ yr^{-1} and the theoretical growth timescale of K-H instability is around 1.5 yr.

The variation from the initial position in the Y-direction can be used to estimate the growth rate of K-H instability in the Y-direction from the MHD simulation. Figures 8(A)–(C) present the variation of the axis of the heliospheric jet from the polar-overhead view and noseward view. With time, the distortion of the axis of the heliospheric jet becomes more significant. The displacement (d), which can be represented as the distance from the original position in the Y-direction, increases over time as shown in Figure 8(D) that plots $\ln(d)$ versus $(t - t_0)$, where t_0 is the initial time corresponding to Figure 8(A). A power-law fit to the modeled values yields $\gamma = 0.14$ with a correlation coefficient $R^2 = 0.986$ (dashed blue line). Therefore, the growth timescale of the K-H instability is

$1/\gamma = 7.1$ yr estimated from the MHD model results, which is consistent with the theoretical lower limit of 2.1 yr.

Figures 9(A)–(C) present the time evolution of the axis of the heliospheric jet in the meridional plane. Figure 9(D) shows $\ln(d)$, the logarithm of the displacement versus $(t - t_0)$, where t_0 is the initial time shown in Figure 6(A). A power-law fit to the modeled values yields $\gamma = 0.18$ with a correlation coefficient $R^2 = 0.986$ (dashed blue line). Therefore, the growth rate of the instability perpendicular to the axis of the heliospheric jet in the meridional plane is $\gamma = 0.18$ and the timescale of it is $1/\gamma = 5.6$ yr. When we coarsen the grid around the area of instabilities from 2 to 4 au, the growth rate γ in the X–Z (meridional) plane becomes 0.16, corresponding to a timescale of $\sim$6.1 yr. In the Y-direction, γ is 0.10 and the timescale is $\sim$9.8 yr. These results are all consistent with the theoretical lower limit on the timescale of 1.5 yr. Further analysis to explore the complexities of instability interactions within the HS will be the focus of future work; including potential interactions and the addition of instabilities such as described in M. Opher et al. (2021).

4. Discussion and Conclusion

In this work, we describe the formation of a low-speed region in the HS due to charge exchange between solar wind and neutral H. The momentum source term generated by the interaction between the solar wind and neutral H decelerates the solar wind speed immediately after the charge-exchange process begins. As a consequence, the TS shrinks, increasing the magnetic field inside the HS. The charge exchange of neutral H with ISM ions creates a wind of 25 km s^{-1}, bending the heliospheric jets. This results in the magnetic field lines and solar wind streamlines no longer being perpendicular but at an angle to each other. The angle between magnetic field lines and solar wind streamlines allows the magnetic tension force to also play an important role in decelerating solar wind inside the HS, especially near the axis of the heliospheric jet. These series of processes explain the formation of the low-speed region within the HS. The low-speed region forms in the solar wind with an ellipsoid shape, providing preconditions for the development of the instabilities inside the HS.

Due to the presence of the low-speed region, shear flows are induced within the HS. This shear flow leads to the generation of the K-H instability within the HS. The growth timescale of the K-H instability in the Y-direction is estimated as $\sim$7.1 yr from the MHD model results, while in the meridional plane, it is $\sim$5.6 yr.

The low-speed region induced by charge exchange serves as a precondition for the development of instabilities in the HS. During the HS evolution, the instabilities along the axis of the heliospheric jet can affect the solar wind speed, magnetic field reconfiguration, and solar wind plasma inside the HS. In future work, we will extend the runtime of the model to analyze the HS instabilities at later times and analyze the effects of the instabilities on turbulence in the heliospheric tail. These results will be key to explaining the large-scale turbulence in the HS and will lead to a deeper understanding of the split-tail structure.

The model used in this paper was based on a single fluid plasma approximation (i.e., the cold thermal plasma and hot PUIs were considered as one fluid). The advanced models used in M. Opher et al. (2020) separate the cold solar wind from the hot PUI ions and found the depletion of PUIs cools the
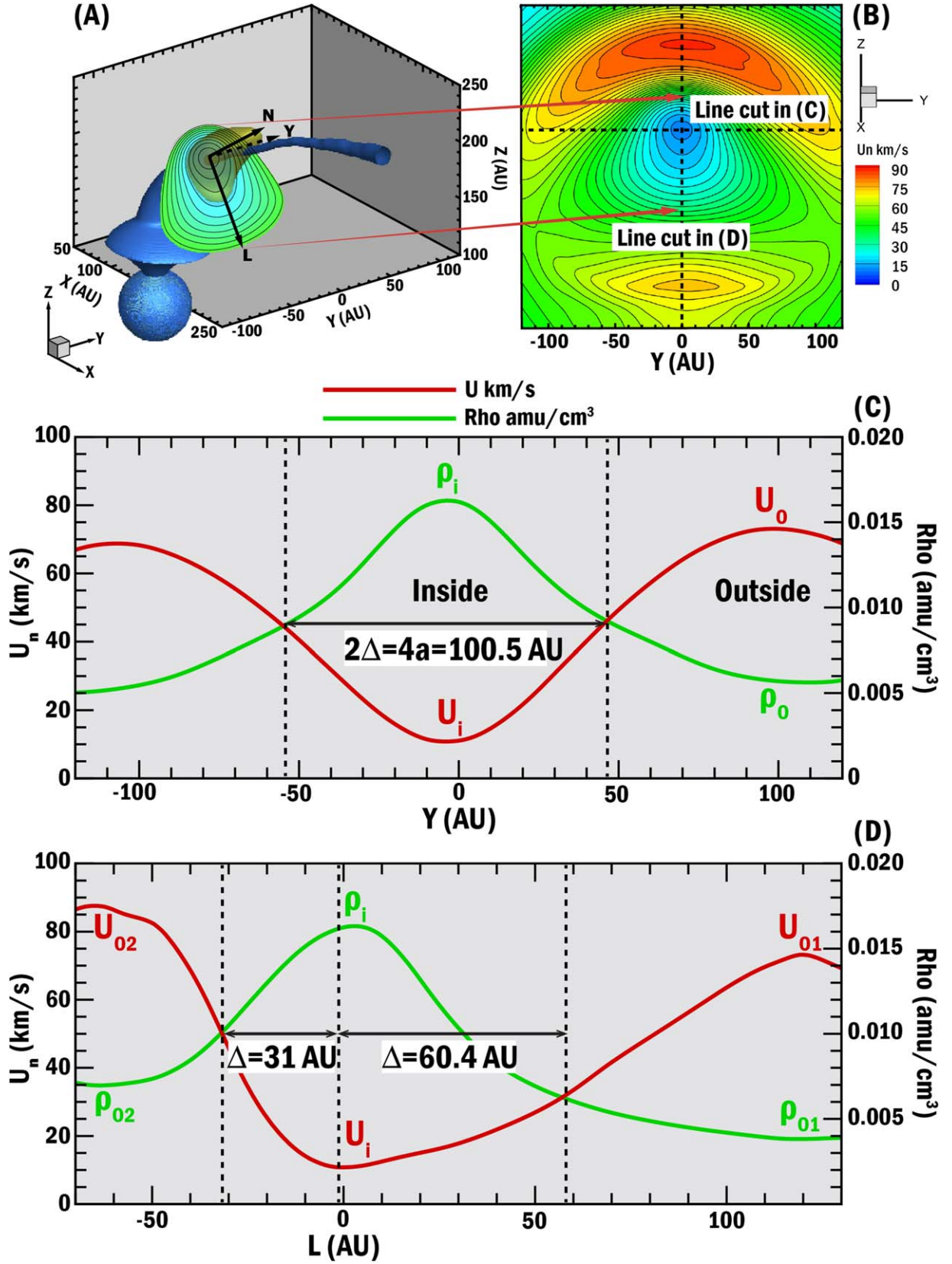
Figure 7. 3D structure of the velocity shear within the HS after the grid refinement at the same time as Figure 6(A). (A) The 3D view of the axis of the heliospheric jet and the low-speed region, along with a cross sectional profile perpendicular to the axis. The directions are illustrated in panel (A), where N is the direction vector of the cross section and L is the direction along the cross section. (B) The total solar wind speed in color contour on the cross section from panel (A). (C) The solar wind density and speed along the line-cut through the heliospheric jet from panel (B) in the Y-direction. (D) The solar wind density and speed along the cut slice perpendicular to the heliospheric jet from panel (B) in the L-direction.
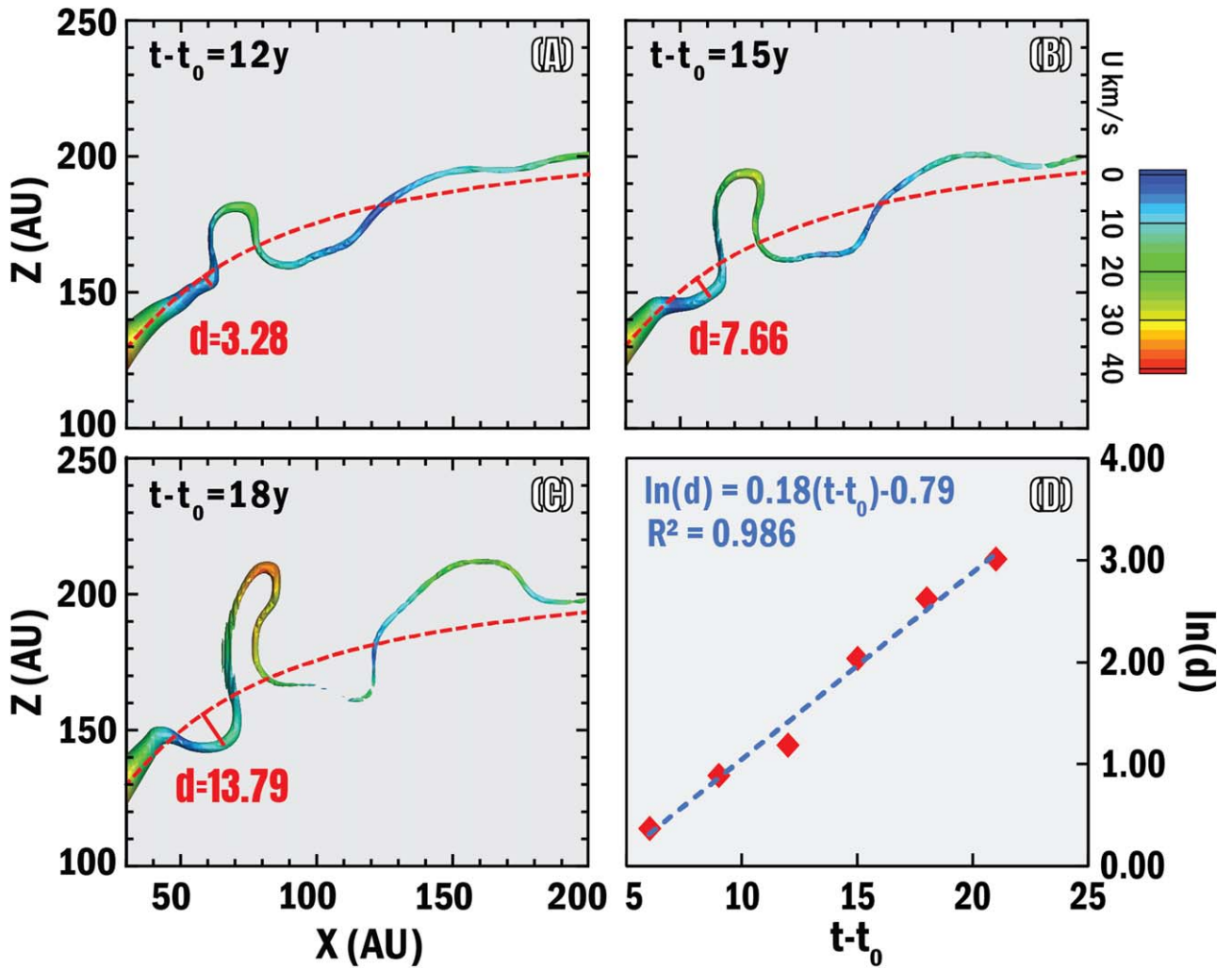
9

Ma et al.
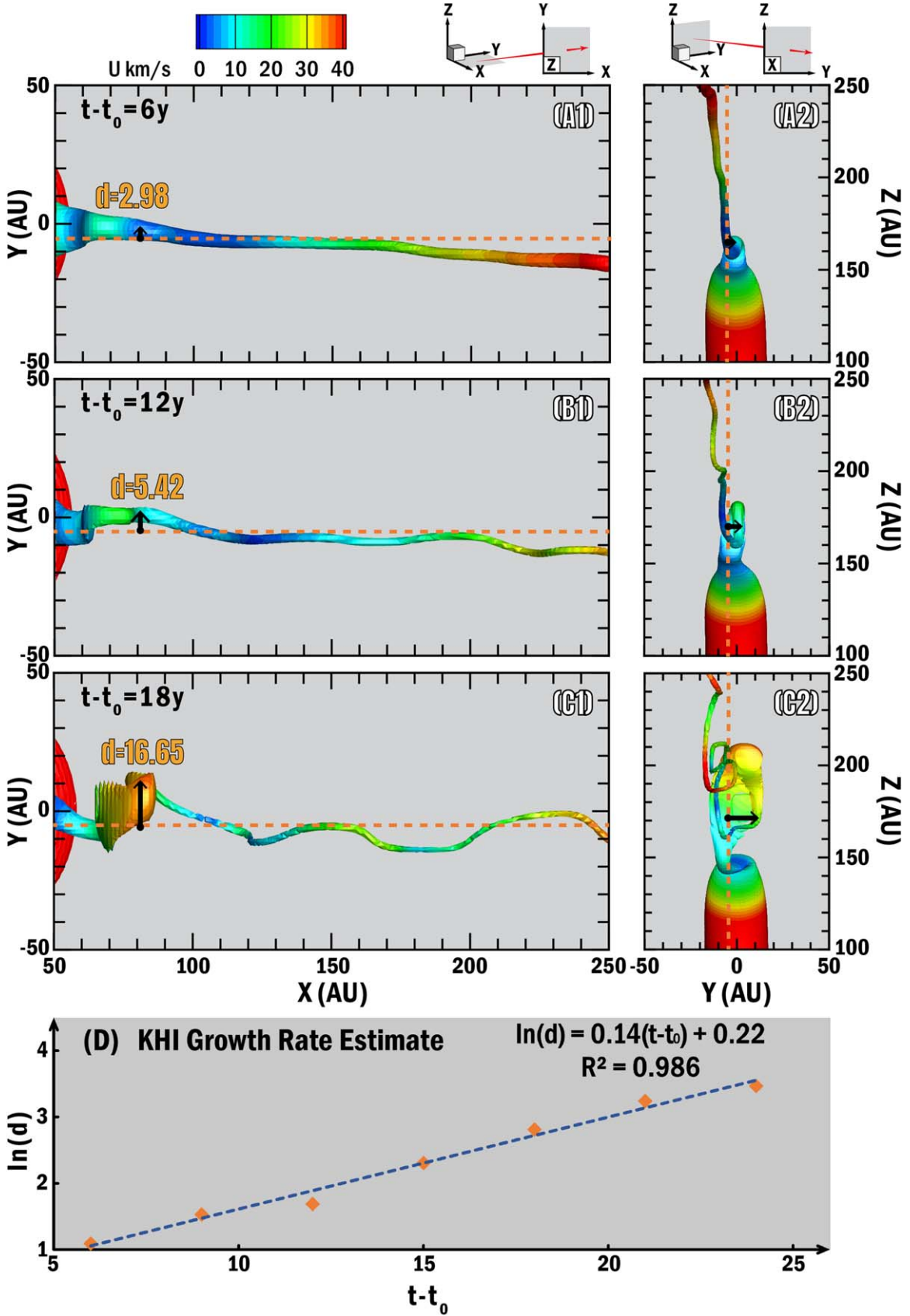
Figure 8. (A)–(C) The displacement of the axis of the heliospheric jet at different times, illustrated by the iso-surface of the solar magnetic field equal to 0.07 nT in the *X–Y* (equatorial) plane and the *Y–Z* (noseward) plane. The color contour on the iso-surface represents the solar wind speed. The dashed orange lines indicate the initial position in the *Y*-direction and the black arrow presents the deviation (d) from it in the *Y*-direction. (D) ln(d) vs. $(t - t_0)$, where (d) is the axis displacement and $t - t_0$ represents the instability growth time. The blue dashed line represents the fit to the measurement data points, shown by orange diamonds.

Figure 9. (A)–(C) The displacement of the axis of the heliospheric jet at different times, illustrated by the iso-surface of the solar magnetic field equal to 0.07 nT in the X–Z (meridional) plane. The color contour on the iso-surface represents the solar wind speed. The dashed red lines indicate the initial position in the meridional plane and the red solid line arrow presents the deviation (d) from it. (D) $\ln(d)$ vs. $(t - t_0)$, where d is the axis displacement and $t - t_0$ represents the instability growth time. The blue dashed line represents the fit to the measurement data points, shown by red diamonds.

heliosphere, "deflating" it and leading to a narrower HS and a smaller, rounder shape. Given that PUIs can play an important role in determining the structure of the heliosphere, they may influence the formation of the low-speed region and subsequently impact the development of instabilities along the axis of heliospheric jets. Future work will investigate how these instabilities are affected when the cooler thermal solar wind ions and the hotter PUIs are treated as separate fluids.

ORCID iDs

Xiaohan Ma https://orcid.org/0000-0003-0007-757X
Merav Opher https://orcid.org/0000-0002-8767-8273
Marc Kornbleuth https://orcid.org/0000-0002-3479-1766
Gabor Toth https://orcid.org/0000-0001-8459-2100

References

Avinash, K., Zank, G., Dasgupta, B., & Bhadoria, S. 2015, JPhCS, 577, 012002
Avinash, K., Zank, G. P., Dasgupta, B., & Bhadoria, S. 2014, ApJ, 791, 102
Baranov, V., Fahr, H. J., & Ruderman, M. 1992, A&A, 261, 341
Baranov, V. B., Krasnobaev, K. V., & Ruderman, M. S. 1976, Ap&SS, 41, 481
Begelman, M. C. 1998, ApJ, 493, 291
Chalov, S. V. 1996, A&A, 308, 995
Chandrasekhar, S. 1961, Hydrodynamic and Hydromagnetic Stability (Oxford: Clarendon)
Drake, J. F., Swisdak, M., & Opher, M. 2015, ApJL, 808, L44
Florinski, V., Zank, G. P., & Pogorelov, N. V. 2005, JGRA, 110, A07104
Fraternale, F., Pogorelov, N. V., & Bera, R. K. 2023, ApJ, 946, 97
Golikov, E. A., Izmodenov, V. V., Alexashov, D. B., & Belov, N. A. 2016, MNRAS, 464, 1065
Izmodenov, V. V., & Alexashov, D. B. 2003, AstL, 29, 58
Izmodenov, V. V., & Alexashov, D. B. 2015, ApJS, 220, 32
Kleimann, J., Dialynas, K., Fraternale, F., et al. 2022, SSRv, 218, 36

Kornbleuth, M., Opher, M., Baliukin, I., et al. 2021, ApJ, 923, 179
Korolkov, S., & Izmodenov, V. 2021, MNRAS, 504, 4589
Korolkov, S. D., & Izmodenov, V. V. 2022, MNRAS, 518, 4422
Liewer, P., Karmesin, S., & Brackbill, J. 1996, JGR, 101, 17119
Miura, A., & Pritchett, P. L. 1982, JGR, 87, 7431
Opher, M., Bibi, F. A., Toth, G., et al. 2009, Natur, 462, 1036
Opher, M., Drake, J. F., Zank, G., et al. 2021, ApJ, 922, 181
Opher, M., Drake, J. F., Zieger, B., & Gombosi, T. I. 2015, ApJL, 800, L28
Opher, M., Liewer, P. C., Gombosi, T. I., et al. 2003, ApJL, 591, L61

Opher, M., Loeb, A., Drake, J., & Toth, G. 2020, NatAs, 4, 675
Parker, E. N. 1958, ApJ, 128, 664
Parker, E. N. 1961, ApJ, 134, 20
Pogorelov, N. V., Borovikov, S. N., Heerikhuisen, J., & Zhang, M. 2015, ApJL, 812, L6
Tóth, G., van der Holst, B., Sokolov, I. V., et al. 2012, JCoPh, 231, 870
Yu, G. 1974, ApJ, 194, 187
Zank, G. P. 1999, SSRv, 89, 413
Zank, G. P., Pauls, H. L., Williams, L. L., & Hall, D. T. 1996, JGRA, 101, 21639